Coalescence-induced jumping of droplets from superhydrophobic surfaces - the effect of contact-angle hysteresis

Physics of Fluids

Coalescence-induced jumping of droplets from superhydrophobic surfaces—The effect of contact-angle hysteresis

Cite as: Phys. Fluids **34**, 113302 (2022); https://doi.org/10.1063/5.0118645
Submitted: 05 August 2022 • Accepted: 03 October 2022 • Accepted Manuscript Online: 08 October 2022 • Published Online: 01 November 2022

K. Konstantinidis, J. Göhl, A. Mark, et al.

Physics of Fluids ARTICLE scitation.org/journal/phf

Coalescence-induced jumping of droplets from superhydrophobic surfaces—The effect of contact-angle hysteresis

Cite as: Phys. Fluids **34**, 113302 (2022); doi: 10.1063/5.0118645
Submitted: 5 August 2022 · Accepted: 3 October 2022 ·
Published Online: 1 November 2022

K. Konstantinidis,[1,a)] J. Göhl,[2] A. Mark,[2] and S. Sasic[1]

AFFILIATIONS

[1]Division of Fluid Dynamics, Department of Mechanics and Maritime Sciences, Gothenburg SE-412 96, Sweden
[2]Fraunhofer–Chalmers Center, Chalmers Science Park, Gothenburg SE-412 88, Sweden

[a)]**Author to whom correspondence should be addressed:** konkonst@chalmers.se

ABSTRACT

Droplets coalesce and jump from superhydrophobic surfaces, a result that stems from the dominance of capillary and inertial forces and the presence of high contact angles. This phenomenon has been a subject of intensive numerical research mostly for cases when the degree of hydrophobicity is described by a single contact-angle value (a static contact angle). The introduction of various degrees of contact-angle hysteresis complicates the numerical modeling of the jumping process due to the sensitivity of the results to the effective value of the contact angle. We have developed and validated a comprehensive volume-of-fluid–immersed boundary numerical framework that accounts for the effect of hysteresis by focusing on the representation of actual (i.e., effective) values of contact angles. By comparing the behavior of jumping droplets on superhydrophobic surfaces with several degrees of hysteresis (up to 15°), we quantified the influence of hysteresis on the jumping process and identified various stages of the merged droplet's detachment and re-attachment to the surface. The latter phenomena were observed in all our simulations with droplets of different initial radii. In all the cases with hysteresis, the merged droplet eventually jumps, but we point out the decrease in the jumping velocity as compared to cases with only a static contact angle imposed. Finally, by using the Kistler dynamic contact-angle model, we demonstrate and quantify the importance of accurately capturing the dynamic receding contact angle when droplets jump from superhydrophobic surfaces with various degrees of hysteresis.

I. INTRODUCTION

The main feature of hydrophobic surfaces is that they inherently resist the contact between a liquid and a solid surface, resulting in a liquid-repellent behavior. The contact angle created at the junction of the three phases, liquid, gas, and solid, is required to be above 150° in order for a surface to be classified as superhydrophobic.[1] Minimization of a liquid–solid contact area has been considered beneficial for numerous applications involving heat transfer with dropwise condensation,[2,3] anti-icing or defrosting coatings,[4–7] water-repellent technology,[8] and self-cleaning surfaces.[9–13] Studies also suggest that avoiding hysteresis, defined as the difference between advancing, θ_{adv}, and receding, θ_{rec}, contact angles, further promotes the use of superhydrophobic surfaces[14,15] in the mentioned applications. However, in practice, the presence of various types of heterogeneities, due to surface roughness and/or wettability discontinuities, can cause deviation from low hysteresis.[16–18] Superhydrophobic surfaces are known for the existence of roughness patterns and heterogeneities caused by hierarchical microstructures (pillars) or anisotropic textures.[1,19] In technological applications, such surfaces are often inspired by natural water-repellent and self-cleaning superhydrophobic surfaces.[13]

Hysteresis is caused by the pinning of the contact line (an intersecting line for liquid, solid, and gas phases) due to defects existing on the surface.[20] The two characteristic angles (advanced and receding ones) are often measured as the limits between which an externally driven droplet remains pinned on the surface.[16] When the contact line starts moving, the dynamics of the moving contact line (MCL) dictate the behavior of the interface and an apparent contact angle, θ_{app}, can be identified at macroscopic scales. The latter angle can exceed the values of θ_{adv} and θ_{rec}. Understood from the physical phenomena at microscopic scales, but with a hydrodynamic description still valid, a dynamic contact-angle model is often formulated.[21,22] A notable characteristic of hysteresis is the pinning force, which is defined as the additional force required to remove a droplet from the surface, before the contact area starts retracting.

The force is computed as $F_{pinning} = 2\sigma R(\cos\theta_{adv} - \cos\theta_{rec})$, where σ is the surface tension of the liquid–gas interface and $2R$ is the droplet diameter given as a reference length.[20]

Self-removing droplets from superhydrophobic surfaces have recently gained attention, since the driving physics of the process is capillarity, a free-energy source. More specifically, when two or more droplets coalesce, they tend to minimize their surface energy, which connects to the minimization of the interface area. The existence of a superhydrophobic surface and its forced interaction with the merged droplet result in redirecting upward the kinetic energy generated during coalescence and cause the eventual jumping of the droplet.[23] This phenomenon has been used for improving performances of various technological applications, such as those involving condensation and self-cleaning of surfaces.[9,24] Numerous experimental and numerical studies have focused on understanding the fundamental mechanisms behind the droplet jumping process. The existence of low adhesion and high contact angles, together with the negligible gravity force for scales smaller than the capillary length, promotes a swift detachment from the surface, reducing the contact area during the jumping process.[25,26] In addition, studies identify distinguished stages of the process, which are the liquid bridge creation and expansion, its interaction with the superhydrophobic surface, the oscillating shapes of the merged droplet resulting from coalescence, and the eventual jumping.[27,28] Boreyko and Chen[23] were the first to observe that condensing droplets can be removed from a surface after coalescing and argued that this phenomenon could significantly improve condensation. The same study provided information on the jumping velocities following a capillary-inertial scaling for droplets of different sizes and presented a cutoff radius for which the droplets in the lower radius region deviate from it. Liu *et al.*[27,28] compared experimental findings of droplets jumping from Leidenfrost surfaces with numerical simulations of droplets jumping on superhydrophobic surfaces. The authors portrayed with this comparison the existence of the already mentioned distinguished stages of the jumping process. Studies on dropwise condensation showed the effect of microstructures on the early release of droplets, which improved the heat transfer.[24,29–31]

A previous study pointed out that the jumping velocity was reaching up to 0.21 v_{CI}, where v_{CI} is the characteristic velocity associated with the capillary-inertial regime.[24] At this velocity, energy efficiency in converting the available surface energy to an upward motion would correspond to 6%, but there are published works that suggest improvements in the efficiency of up to eight times in the case of structures located between the coalescing point and the surface.[32–35] However, most studies suggest a certain range of jumping velocities ($v^*_{jump} = 0.2$–$0.25\ v_{CI}$)[24,26,36,37] and energy conversion rates (from 3% up to 6%). Yan *et al.*[38] performed a systematic study of the differences in jumping resulting from different surface structures, wettabilities, and relative sizes of droplets. Their findings suggested a maximum jumping velocity of 0.26 v_{CI} for two droplets coalescing on a superhydrophobic surface with nanoblade structures. For surfaces with microscale textures or wettability changes, the same authors identified variations in the jumping direction, and the jumping velocity reported was generally scattered from the capillary-inertial scaling and reduced for the biphilic surface.

Jumping of droplets on superhydrophobic surfaces has also been investigated numerically. From the realm of continuum-based techniques that focus on capturing or tracking the interface, volume of fluid (VOF) was mostly selected[33,42,43,45,47–51] even though several other methods were also used.[44,52–54] In addition, there are studies using either a lattice Boltzmann framework[40–42,55–57] or molecular dynamics[57–59] with results that in principle showed the same trends and observations as did the experiments and continuum-based simulations. This matching of findings is related to the overall characteristics of the jumping process, but also to the relevance of the proposed capillary-inertial scaling law.[23] A comparative list for the jumping velocities, that are obtained upon detachment and range in the main body of the capillary-inertial region, given by both numerical and experimental studies, is presented in Table I. The given values are normalized by $v_{CI} = \sqrt{\sigma/(R_i\,\rho)}$.

There has been a relatively limited number of numerical works that varied the value of the contact angle (often referred to as the static or the equilibrium contact angle) and consequently displayed a different velocity behavior for the droplets during jumping.[43] This variation in the results demonstrates the sensitivity of the problem and stresses the importance of accurately modeling the dynamics of the moving contact line (MCL). The fact that the eventual jumping velocity is sensitive to the value of the contact angle suggests that the presence of hysteresis will indeed influence the entire droplet jumping process and therefore necessitates that a trustworthy contact–angle representation is considered during the implementation of boundaries. Cheng *et al.*[53] looked at this phenomenon and noted that, by varying the contact angle and assuming constant values for θ_{adv} and θ_{rec}, the process of jumping was mostly influenced by the value of the receding contact angle. We also note that the velocity results of a no-hysteresis configuration reported in that study show differences as compared with the majority of the published numerical results related to the evolution of the jumping velocity. More specifically, the expected stages of the jumping process were not clearly observed in the results. Another work by Chen *et al.*[44] used the generalized slip boundary condition to connect the contact line velocity with a dynamic contact angle, but the effect of hysteresis was investigated by varying a slip parameter while not showing how the model compared to a no-hysteresis case. Nam *et al.*[60] compared the jumping behavior of a hydrophobic and a superhydrophobic surface with dynamic contact angles in order to identify dissipation of the MCL due to hysteresis-induced pinning and viscosity. In an experimental study, Cha *et al.*[61] performed experiments with superhydrophobic surfaces of different textures and with variable contact angles and degrees of hysteresis. The authors identified different minimum droplet sizes for the jumping to take place and pointed to pinning and no-jumping observations as the outcomes of an increased droplet–surface adhesion in the cases with a more pronounced hysteresis. A noble guess for the adhesion effect, which has also been mentioned previously,[60] would be that a higher degree of hysteresis permits lower receding angles to occur when the droplet retracts from the surface. The adhesion force to the surface should also reduce the efficiency of the jumping process.[61] Experiments have not yet reported the actual values that the apparent contact angle obtains during the stages of droplet coalescence and jumping on superhydrophobic surfaces. This statement represents a limitation when promoting the use of a certain tested dynamic contact angle model. Instead, those values are often provided from experimental studies as the θ_{adv} and θ_{rec} from initial arrangements of droplets before initiation of the contact line movement. Finally, another study by Attarzadeh and Dolatabadi,[42] which investigated numerically the effect of microstructures on

TABLE I. List of the reported numerical and experimental jumping velocities of merged droplets on superhydrophobic surfaces.

Numerical										
Authors	Liu *et al.*[27]	Farokhirad *et al.*[39]	Liu and Cheng[40]	Khatir *et al.*[37]	Wang *et al.*[41]	Attarzadeh and Dolatabadi[42]	Wasserfall *et al.*[43]	Vahabi *et al.*[33]	Tryggvason[44]	Li *et al.*[45]
Normalized jumping vel. (–)	0.20	0.20	0.18	0.18–0.20	0.18–0.23	0.20	∼0.25	0.20	0.22	0.22

Experimental								
Authors	Boreyko and Chen[23]	Liu *et al.*[28]	Enright *et al.*[24]	Kim *et al.*[36]	Khatir *et al.*[37]	Mouterde *et al.*[46]	Wang *et al.*[26]	Yan *et al.*[38]
Normalized jumping vel. (–)	0.19	0.21	∼0.21	0.23	0.16–0.19	0.17–0.25	∼0.20–0.24	0.26

superhydrophobic surfaces, mentions the use of θ_{adv} and θ_{rec} as upper and lower limits of their contact-angle implementation. For a flat surface without such structures, the $\Delta\theta$ was selected to be around 3°. For the heterogeneous surface with rectangular pillars, the same authors used the Kistler dynamic contact-angle model with a static contact angle as input. However, there were no investigations for scenarios with higher degrees of hysteresis.

Our interest in this work is mainly inspired by the possibilities of tuning and improving superhydrophobic surfaces through simulations that are capable of predicting the effective (i.e., truly acting) values of contact angles. We note that such an analysis is possible even when surfaces are modeled as flat surfaces, that is, when heterogeneities are not explicitly a part of the computational domain. For that purpose, it is only important that the simulations are able to correctly model the physics of a droplet–surface interaction and predict scenarios when dynamic contact angles are affecting the jumping process. The acquired knowledge can be used to tailor superhydrophobic surfaces to, for example, facilitate and promote jumping for specific droplet sizes that are considered advantageous for certain applications and that would not jump on every superhydrophobic surface.[31,61,62] Additionally, we can use the suggested numerical framework to identify the exact tuning characteristics that would help to minimize the adhesion force. This would increase the energy conversion rate of the merged droplet's upward motion. Numerous applications will also benefit from monitoring and controlling the effect of hysteresis since the observed contact angles on newly designed superhydrophobic surfaces are related to the potential overall efficiency of the jumping process with a framework that handles the contact-angle hysteresis by paying special attention to fine details of the moving contact line (MCL) dynamics. However, we point out the absence of credible proof that a certain dynamic contact-angle model would in general behave more accurately than any of the ones typically presented in the literature, without limiting our discussion to just the implementations relevant for our work. Additionally, we argue that the representation and implementation of the actual contact angles become more challenging but also more important, because the outcome of the whole process is highly sensitive (as we will show in what follows) to the droplets' interaction with the surface. For making possible optimization of the properties of a superhydrophobic surface through numerical simulations and in order to achieve a high degree of accuracy when predicting the dynamics of the MCL, special treatment is required in the numerical framework to deal with the existence of the stress singularity at the MCL.[63–65] For that purpose, we use in this work the frequently suggested Navier slip boundary condition[66,67] and implement it in the way as described in Sec. II.

Although a specific behavior of jumping droplets on surfaces with hysteresis has already been observed experimentally, there is still a lack of numerical analyses that focus on the details of the droplet–surface interaction and the contact line movement in such cases. Moreover, there is still a limited number of studies that provide detailed explanation and quantification of the changes in the jumping behavior that the presence of hysteresis may cause. The present work is an attempt to fill that gap, and for that purpose, we use the in-house multiphase flow solver IPS IBOFlow®. The solver is based on a comprehensive combined VOF–immersed boundary framework and includes several dynamic contact-angle models and a Navier slip model, as presented and validated by Göhl *et al.*[68] To understand the behavior of jumping droplets on superhydrophobic surfaces with a significant hysteresis present, realistic values for θ_{adv} and θ_{rec} from selected experimental works are used and variations in the degree of hysteresis are performed to identify limitation points. For the contact-angle implementation, our idea has been to increase gradually the complexity with which hysteresis is both introduced and modeled on the studied superhydrophobic surfaces. We thus start with an implementation of fixed advancing and receding contact–angle values using the quasi-static scheme, and continue with an example of a selected dynamic contact-angle model. In summary, we aim at identifying, understanding and quantifying a range of behaviors for jumping droplets when different degrees of hysteresis are present. For that purpose, we carry out a systematic numerical investigation on how the presence of hysteresis affects the jumping process by looking at the detailed physics of the contact angles and the MCL, and the influence of the radii of the involved droplets.

II. METHODOLOGY AND CONFIGURATION

A. Methods

The numerical computations were performed with the in-house flow solver IPS IBOFlow® that is based on a combined volume-of-fluid

(VOF)–immersed boundary method.[69] It solves the incompressible Navier–Stokes equations

$$\nabla \cdot \mathbf{v} = 0\,, \qquad \frac{\partial(\rho \mathbf{v})}{\partial t} + \mathbf{v} \cdot \nabla(\rho \mathbf{v}) = -\nabla p + \nabla \cdot (\mu \nabla \mathbf{v}) + \rho\, \mathbf{g} + \mathbf{f}_{SF}, \tag{1}$$

where $\mathbf{v}$ gives the velocity vector field, P the pressure, ρ and μ are the density and dynamic viscosity of the fluid, $\mathbf{g}$ is the gravitational acceleration, and $\mathbf{f}_{SF}$ is the surface tension force at the interface.

VOF is a sharp interface-capturing method and includes a transport equation for the volume fraction field to capture the interface location, which reads

$$\frac{\partial \alpha}{\partial t} + \mathbf{v} \cdot \nabla \alpha = 0, \tag{2}$$

where α is the volume fraction. Additionally, to obtain the fluid properties for a volume cell, density and viscosity are computed by the volume average of the properties for the two fluids as follows:

$$\rho = \alpha\, \rho_1 + (1 - \alpha)\, \rho_2, \tag{3}$$

$$\mu = \alpha\, \mu_1 + (1 - \alpha)\, \mu_2. \tag{4}$$

The coupling of pressure and velocity is performed with the help of the segregated SIMPLEC method,[70] and the discretization is performed on a co-located grid. For the volume fraction equation, Eq. (2), discretization of the advective part is performed according to the higher order differencing scheme CICSAM.[71] It is a fully conservative and bounded scheme that ensures sharpness of the interface during its advection.

The continuum surface force method (CSF)[72] is used for the surface tension body force $\mathbf{f}_{SF}$, where the force is given from the interface geometry and the surface tension property as

$$\mathbf{f}_{SF} = \sigma \kappa \mathbf{n}, \tag{5}$$

where σ is the surface tension between liquid and gas, κ is the interface curvature, and $\mathbf{n}$ the interface normal vector.

The unit normal vector $\hat{\mathbf{n}}$ for the interface is computed from the gradient of the volume fraction, whereas the curvature is obtained from the divergence of $\hat{\mathbf{n}}$,

$$\hat{\mathbf{n}} = \frac{\mathbf{n}}{||\mathbf{n}||} = \frac{\nabla \alpha}{||\nabla \alpha||}, \tag{6}$$

and then the curvature is calculated as

$$\kappa = -\nabla \cdot \hat{\mathbf{n}}. \tag{7}$$

To capture the location of the moving contact line and model the angle of the interface, the following approach is used: for numerical implementation of the contact angle, we follow our previous work.[68] For the implementation of hysteresis with different advancing and receding contact angles, the quasi-static model is used that imposes the apparent contact angle by recognizing a receding or advancing movement in accordance with the computed contact line velocity. In addition, we use the Kistler dynamic contact–angle model and the value of the imposed dynamic contact angle θ_{dyn} in the cells near the solid surface and in proximity to the location of the contact line is given as follows: it is known that Kistler's law, as it is also known, applies the Hoffman function f_{Hoff},[73,74] which is a correlation to experimental data, when the contact line velocity is to be calculated. When using the Kistler model, the value of the contact angle for a static arrangement is required, which is the same as the quasi-static θ_{adv} and θ_{rec} values for the corresponding contact line movement. In this study, we thus adopt that the angle for a stationary contact line in the Kistler model is given by the advancing or receding contact angles, as they are available from experimental studies. Then, a modification of the Hoffman function was performed following a study on both advancing and receding contact angles, which demonstrated that, for surfaces with very high contact angles,[75] the Kistler model is still able to capture the behavior of the reported experimental data.[74] The equation reads

$$\theta_{dyn} = f_{Hoff}\left(Ca + f_{Hoff}^{-1}(\theta_{st})\right), \tag{8}$$

where

$$f_{Hoff}(x) = \cos^{-1}\left(1 - 2\tanh\left[5.16\left(\frac{x}{1 + 0.332x^{0.99}}\right)^{0.62}\right]\right). \tag{9}$$

As all solution variables are stored at the cell centers, a balanced-force method[76,77] is used to improve the accuracy of the properties calculated at the faces. This method includes the forces and a time derivative in the velocity interpolation, making the forces and the pressure gradients balanced at cell faces. The result is a more accurate and stable estimation for the face velocities, reducing the spurious currents and oscillations due to pressure instabilities.

Boundary conditions are formulated using the mirroring immersed boundary method (MIBM)[69,78] that makes it possible to describe solid surfaces with triangulated objects. MIBM is a second-order accurate method that sets the velocity field at the boundary by mirroring the velocity field. The method is used to set the local boundary condition on the structured octree-background grid. For the contact line, the method simplifies the surface force calculations when considering the local boundary normal vector needed when implementing a contact-angle model.[68]

For the velocity at the three-phase boundary, a slip effect is assumed and modeled with the Navier slip boundary condition to remove the MCL stress singularity problem. Following the implementation of the immersed boundary method in our previous publications,[68,79] the slip velocity is computed in the tangential direction and imposed by the immersed boundary condition in the equation of MIBM that reads

$$\frac{\vec{v}_{ext} + \vec{v}_{ghost}}{2} = \vec{v}_{IB,slip}, \tag{10}$$

where $\vec{v}_{IB,slip}$ is the computed velocity to be set at the boundary for which the tangential slip velocity v_{slip} has been added, $\vec{v}_{ext}$ is the velocity at the nodes of the fluid, and $\vec{v}_{ghost}$ is the velocity at the fictitious nodes of the domain that are occupied by the body mass.

B. Configuration of the simulations

We design our simulations in three Cartesian dimensions with a flat plane representing the superhydrophobic surface for which the boundary conditions are imposed. The framework has the ability to vary the number of droplets and their sizes. In addition, it connects the grid creation and the domain dimensions to the radius of the smallest droplet. The size of the domain is $10R_i \times 8R_i \times 6R_i$, scaling to the smallest droplet initial radius R_i, as represented in Fig. 1(a).

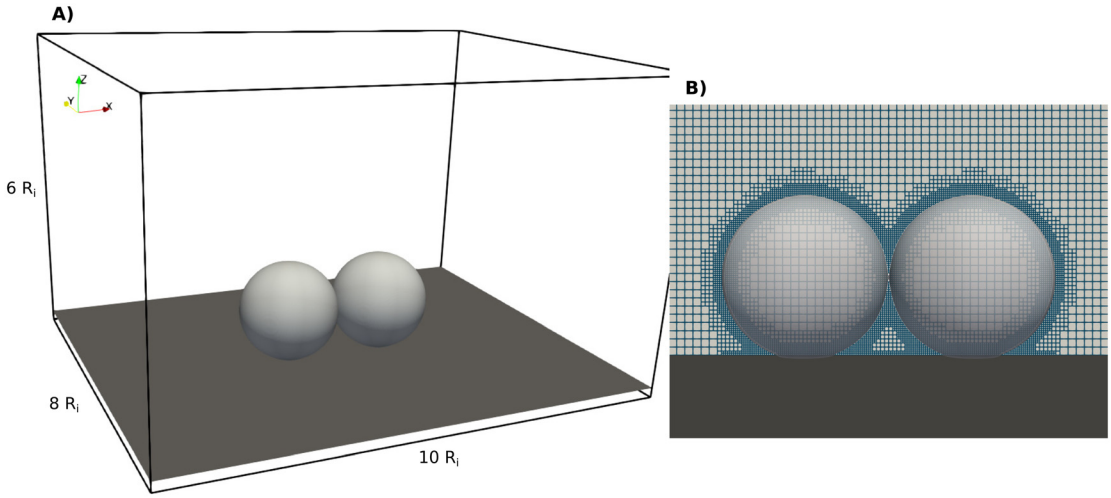

FIG. 1. Representation of (a) the physical model used in our work and (b) the grid setup and refinement for a case for which the minimum cell size is 1/40 of R_i. (40 cells per R_i)

The grid is automatically created with an octree grid that uses adaptive grid refinement (AGR). The method is setting a selected level of refinement to the interface between the fluids, as well as to the liquid–solid boundary. The AGR method monitors the interface at every time step and, depending on movements of the interface, updates the grid if needed. It sets at least six cells of the highest refinement level stretching away from the interface [see also Fig. 1(b)]. These cells are selected to have a size proportional to R_i. For example, when a certain grid is said to have 20 cells per $R_i(c_R)$, where $\Delta x = R_i/c_R$, this expression implies that the cells near the interface have a cell size corresponding to 1/20 of the droplet radius. The same principle of course holds for other grid resolutions.

The choice of a time step in a problem with a high influence of capillary and inertial forces needs to take into account the dominating time scales for the jumping droplets phenomenon. The time is given as the normalized time τ, which is scaled by the capillary-inertial timescale t_{CI}, and hence, the time step Δt should be smaller than $t_{\mathrm{CI}} = \sqrt{R_i^3 \rho/\sigma}$. In addition, the time step needs to respect the time step constraint related to capillary waves

$$\Delta t \leq \sqrt{\frac{(\rho_1 + \rho_2)\Delta x^3}{4\pi\sigma}} \tag{11}$$

as derived by Brackebill *et al.*[72] or the equivalent one suggested by Denner and van Wachem[80] for a static case of oppositely coming waves

$$\Delta t \leq \sqrt{\frac{(\rho_1 + \rho_2)\Delta x^3}{2\pi\sigma}}. \tag{12}$$

Additionally, the time step choice must comply with the Courant number (CFL) condition. For different droplet radii, the average normalized jumping velocity is considered constant $v^*_{jump} = U$, as has been shown by several previous works.[27,39] The velocity in the capillary-inertial regime scales with $v_{\mathrm{CI}} = \sqrt{\sigma/(R_i\,\rho)}$. So, the actual average jumping velocity should be $v_{jump} = U\,v_{\mathrm{CI}}$. When a default case is set up for the system with Δt_{def} being the time step and $\Delta x_{def} = R_{i,def}/c_{R,def}$, we have the Courant number computed as

$$\mathrm{CFL}_{def} = \mathrm{CFL}_{const} = \frac{v_{jump}\,\Delta t_{def}}{\Delta x_{def}}. \tag{13}$$

To reach a constant CFL when the radii of the initial droplet or the cell size vary, the time step needs to be adjusted so as

$$\Delta t = \mathrm{CFL}_{const}\frac{\Delta x}{v_{jump}}. \tag{14}$$

By substituting in Eq. (14) the definitions for v_{jump} and Δx_{def}, the time step of a simulation with different R_i or grid resolution should follow:

$$\Delta t = \Delta t_{def}\left(\frac{R_i}{R_{i,def}}\right)^{\frac{3}{2}}\frac{c_{R,def}}{c_R}. \tag{15}$$

III. VALIDATION

We demonstrate time convergence of our framework by following the jumping of two equally sized droplets of $R_i = 25\,\mu$m and using three time steps for the simulations, $\Delta t = 2.5 \times 10^{-8}$, 1.25×10^{-8}, and 0.625×10^{-8} s, that correspond to maximum Courant–Friedrichs–Lewy (CFL) values of approximately 0.55, 0.30, and 0.15, respectively. Figure 2 shows the evolution of the velocity profile with time τ and velocity v^* normalized by the corresponding scales t_{CI} and v_{CI}, respectively. The lines show an identical velocity evolution for the different time steps, as no observable difference between them is identified. That would in theory permit us to use the largest time step of the three cases for all our simulations. However, due to an excess increase in the number of inner iterations for reaching the same solution residual, doubling the time step is not accompanied by halving the computational cost and, as a result, the medium time step of $\Delta t = 1.25 \times 10^{-8}$ s was selected for use throughout this work. Moreover, the selected time step case returned values for the Courant number that do not exceed 0.5 for all the simulations performed in this study. Restricting CFL preserves a sharper estimation of the interface from the CICSAM method, which will retain the same approach for computing convective coefficients in the volume fraction transport equation.

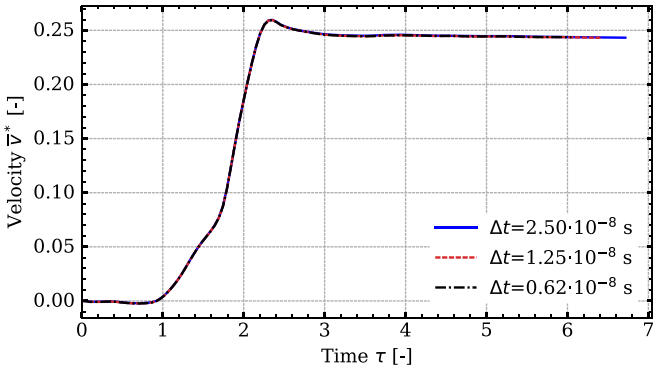

FIG. 2. Time convergence study of the average upward velocity in time, normalized by the capillary-inertial scales. The radius of the initial droplets is 25 μm.

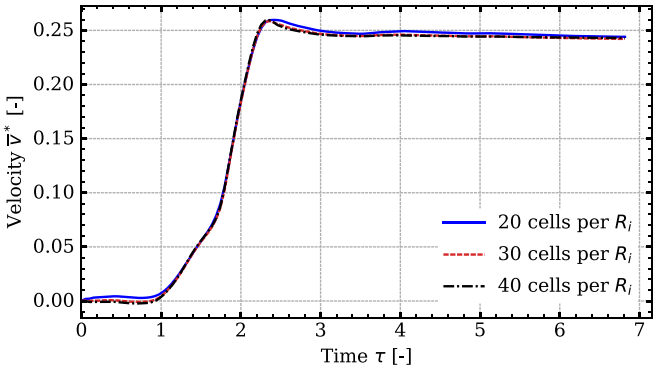

FIG. 3. Grid convergence study of the average upward velocity in time, normalized by the capillary-inertial scales, for three different grid configurations for $R_i = 25\ \mu$m. The cases involving 30 and 40 cells per R_i demonstrate convergence of the jumping velocity behavior.

To achieve and prove grid convergence, it is needed to understand the behavior of the slip length l_{sl} that is used in the formulation of the Navier slip boundary condition. A series of tests were performed to identify the sensitivity of the simulations to the grid resolution. Studies show that in several applications the slip length is highly dependent on the cell size of the cells in the vicinity of the solid surface.[81,82] For the jumping droplets case, the slip length can be also associated with the radius or another characteristic length of the system, for example, the height of superhydrophobic microstructures. Therefore, we tested two methodologies to identify how grid convergence and the outcome of the jumping process are affected by the choice of a slip length. By varying the cell size, we observed that in the cases when the slip length was adjusted to a half of the cell size, grid convergence was partly achieved but with a distinct separation between the jumping droplet velocities. Second, when the slip length was kept constant in relation to the droplet radius, convergence was achieved consistently in the jumping velocities with a better agreement of the final result. The general behavior of the system was similar for all the simulations, but to our understanding, the slip length is an important parameter to identify the instant when the droplet is released from the solid surface.

We present the results from the simulations with 20, 30, and 40 cells per R_i, with a slip length of $l_{sl} = 310$ nm and $R_i = 25\ \mu$m. In Fig. 3, the cases of 30 and 40 cells per R_i show convergence, while the case of 20 cells per R_i does not yield the same result. For the remaining simulations in this paper, the resolution of 40 cells per R_i is selected. The proposed grid configuration is benefiting from the use of two levels of refinement close to the interface. To keep an acceptable size of the cells in the regions that exclude the interface and the moving contact line (termed base cells), only a single level of refinement is suggested for use in a coarser grid. For the case of 30 cells per R_i, the base cells in the far domain are smaller than for the 40 cells per R_i case, increasing the computational cost in the less significant regions of the domain in the far-field of the interface.

We also compared the results of our simulations to experimental results of the jumping velocity. In Fig. 4, data from Yan *et al.*[38] are presented for the jumping velocity measured upon detachment, normalized by the capillary-inertial velocity scale v_{CI} for different initial droplet radii R_i. The mentioned study provides consistent measurements of the jumping velocity that follows the capillary-inertial scaling. The simulations were performed using advancing and receding contact angles $\theta_{adv} = 170.3°$ and $\theta_{rec} = 167.7°$ that correspond to the measured values of the homogeneous superhydrophobic surface in the experiment. A good agreement of the jumping velocities is noticed, with the numerical results overall capturing the behavior observed in the experiment. The trend of the normalized jumping velocity to remain constant over R_i for the capillary-inertial scaling is clearly demonstrated in our simulations. The estimated jumping velocity is lower only by less than 5% compared to the experimental mean value. We seem to marginally underpredict the exact value of the experimental results, for which the reasons can be various. We argue that one of the reasons could be because we cannot be entirely certain regarding the fluid properties or the reported droplets radii in the experiments. It is to be noted here that the slip length used in the simulations was equal to the size of a wall cell, in the 40 cells per R_i grid, for the simulation case with initial droplets of size $R_i = 288\ \mu$m. This approach returns a physical value of $l_{sl} = 7.2\ \mu$m and the chosen setting gave the best agreement with the experiment for our jumping velocity, while such a

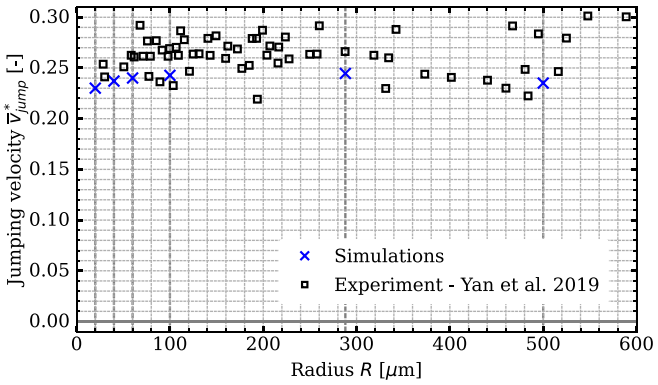

FIG. 4. Obtained jumping velocities from the simulations with different droplet radii R_i as compared to experimental data by Yan *et al.*[38] Both sets of values are normalized with the corresponding velocity capillary-inertial scale v_{CI}.

high slip length is in line with the observed properties of superhydrophobic surfaces.[19]

An extra emphasis is now given to demonstrate the adaptivity and high fidelity of our framework, by performing a three-droplet simulation of jumping of unequally-sized droplets. The aim here is to reproduce in detail all the stages of this process as shown in the experimentally obtained images presented by Yan *et al.*[38] We have estimated the radii of the initial droplets as $R_1 = 235\ \mu$m, $R_2 = 268\ \mu$m and $R_3 = 293\ \mu$m by analyzing the published figure and the suggested scaling from the authors. Time instants are presented with the simulation results matching the experimental images in Fig. 5. An exceptionally close agreement is demonstrated between the complex droplets' oscillation features appearing in the experiment and the video produced by our simulation. In detail, the initial process of the two larger droplets coalescing and the smaller one remaining still is unambiguously recognized in both the simulation and the experiment. At the moment when the smaller droplet starts its own coalescence with the resulting droplet, the expansion of the liquid bridge seems to agree for the two cases, as does the general shape of the two pre-merged droplets. Next, the expansion in the lengthwise direction and the liquid bridge formation is captured properly. The two recognizable features (lump-shaped formations) from the pre-merged droplets and the smaller droplet exist in all the instants following up to the point when the smaller droplet merges to the already formed bigger formation. The nipple formation has been accurately modeled by the simulation and at the correct time scales. When the jumping occurred, only a single instant was provided in the experimental study, which our simulation managed to predict as well. Therefore, we argue that the overall behavior of the jumping process for the three unequal droplets has been captured with very good precision. Consequently, we recognize the ability of our framework to capture the behavior of strong inertial and capillary effects that exist in the jumping droplets phenomenon.

We finally provide a validation case that reflects the nuances that the presence of hysteresis brings to a jumping droplets process. We first note that a general lack of significant quantity of experimental data on such surfaces (and especially on the parametric details that such studies could uncover) renders comparisons between experiments and numerical simulations far from straightforward. In our work, we have chosen to rely on a qualitative comparison with an experimental video provided as video S4 in the supplementary material of Yan *et al.*[83] The reported surface had a hysteresis of $\Delta\theta = 17^\circ$, with $\theta_{adv} = 162^\circ$ and $\theta_{rec} = 145^\circ$, and the radius of droplets of $R_i = 156\,\mu$m. In Fig. 6, a set of instances extracted from that video are compared to our simulation with the same contact-angle values. The contact-angle model used for the simulation in this case was the quasi-static model, which was found to have a similar pinning moment at the fifth instant (at $t = 9.9 \times 10^{-4}$ s) shown in the figure. We point to the nucleation of tiny droplets in the experiments, as the surface was reported to be cooled. The existence of these droplets does not affect the experimentally identified stages of the jumping droplets process. We recognized in our simulations the same patterns in the oscillations and formations of the merged droplet as those in the experiment. Hence, we consider our numerical framework validated also for dealing with superhydrophobic surfaces with various degrees of hysteresis present, in addition to being able to capture the shape oscillations caused by the dominance of capillary and inertial forces.

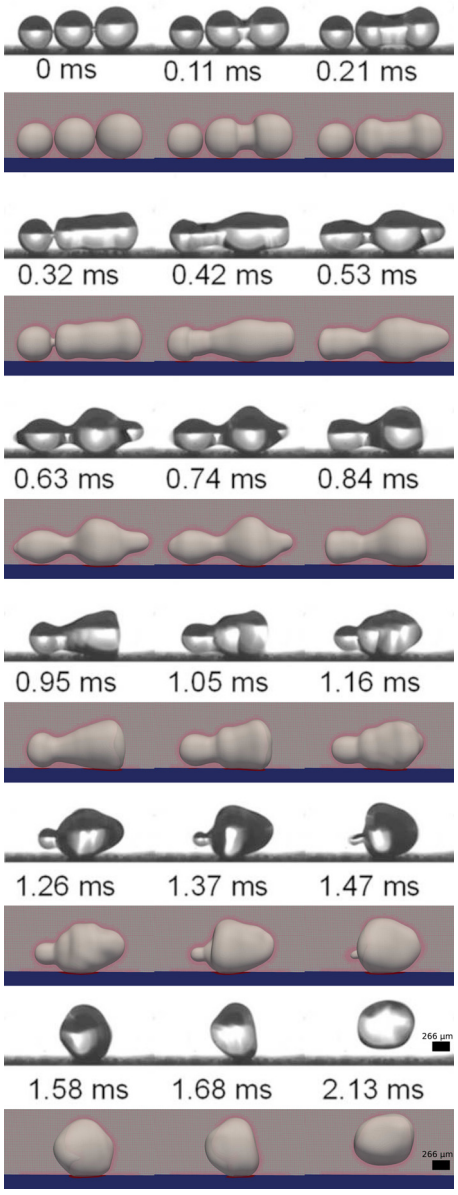

FIG. 5. Comparison of different stages of the coalescing and jumping of three unequal droplets, provided by our simulations and experiments by Yan *et al.* [reproduced with permission from Yan *et al.*, "Droplet jumping: Effects of droplet size, surface structure, pinning, and liquid properties," ACS Nano **13**, 1309–1323 (2019)].[38] The images from experiments are always given above the corresponding simulation ones. The droplet sizes are indicated in the bottom of the figure.

IV. RESULTS AND DISCUSSION

To understand the influence of contact-angle hysteresis on the jumping process, we have carried out a series of simulations with various degrees of hysteresis and under different operating conditions. A qualitative point of comparison and a starting point in our analysis are to create numerical cases in accordance with existing experimental studies of droplets jumping from superhydrophobic surfaces with

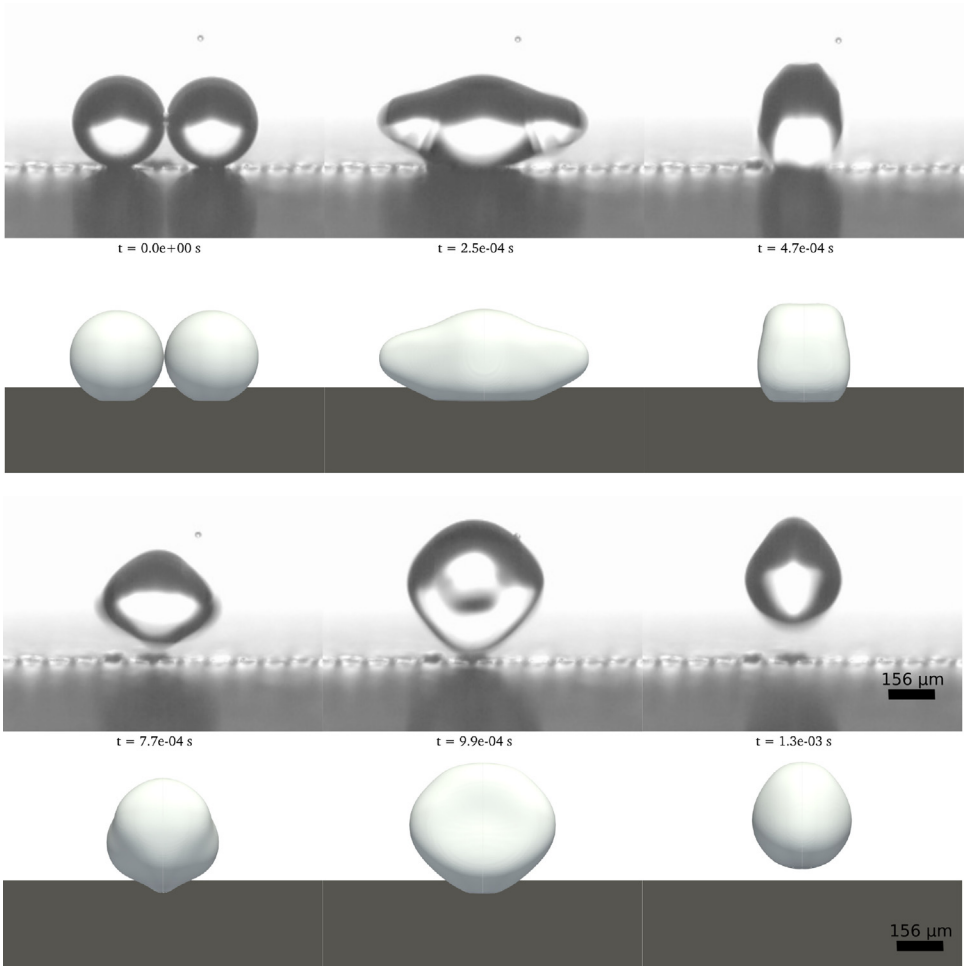

FIG. 6. Validation case of droplets jumping from a superhydrophobic surface with hysteresis present, as provided by a video recording from Yan *et al.* [reproduced with permission from Yan *et al.*, "Droplet jumping: Effects of droplet size, surface structure, pinning, and liquid properties," ACS Nano **13**, 1309–1323 (2019)].[83] The images from the experiments are given above the corresponding simulation ones, and instants from the simulation are provided that match the recording video timing suggested from the authors of the cited experimental study. Droplet sizes are indicated in the bottom of the figure.

non-negligible degrees of hysteresis. Following the study of Mulroe *et al.*[31] that reported on the jumping ability of droplets with different radii from tuned superhydrophobic surfaces, we have selected a surface with a high degree of hysteresis as our base case. For the presented surface, designated as *S3* in Mulroe *et al.*,[31] the values of $\theta_{adv} = 162°$ and $\theta_{rec} = 147°$ are provided. A minimum reported radius, termed a cutoff radius of droplets that indeed jumped on the *S3* surface, was approximately 25 μm. We recreated such a case with equal droplets and first used the quasi-static contact-angle model to study the moving contact line. A simulation with a static contact angle of $\theta = (\theta_{adv} + \theta_{rec})/2$ was also performed in order to understand how a simplified modeling approach for the contact angle would influence the jumping process. The two cases confirmed coalescing and jumping from the surface, but significant differences were observed. The results are presented by a plot of the normalized velocity evolution in Fig. 7. Additionally, five instants of the two simulated cases are shown in the figure. We note that the stage of the liquid bridge expansion and the initial oscillations is captured similarly for the two cases. As depicted at instant *I*, the contact area with the solid surface is roughly the same, as well as the shape of the merged droplet. It can be also observed that during the liquid bridge expansion, the initial contact area of the droplets reduces, causing a receding behavior at the contact line of the two initial droplets with the solid surface. While it later reaches roughly the same average upward velocity, the simulation with hysteresis has a higher degree of initial attraction toward the surface, probably caused by the enforcement of the receding contact angle "sticking" the two initial droplets to the solid surface. This θ_{rec} is reduced by 7° compared to the value of the static contact angle imposed in the no-hysteresis case, where the contact angle is given by its equilibrium value. As expected from the literature, at instant *II* the droplet in a no-hysteresis case detaches from the surface. In contrast, the droplet with the hysteresis present retains contact with the surface due to the action of the receding contact angle (note the difference in the droplet–surface contact area at instant *II* for the two cases in Fig. 7). Following a period where the velocity keeps decreasing for the hysteresis case, at instant *III* the merged droplet was also detached from the surface. It is noted that the shape of the droplet shows characteristic variations compared to the elevated no-hysteresis case. At instant *IV*, the merged droplet for the simulation with hysteresis re-attaches to the surface during a shape oscillation, in which the droplet elongates in the vertical direction and the interface hits the solid surface. Contact angles are re-applied, and the velocity of the merged droplet decreases.

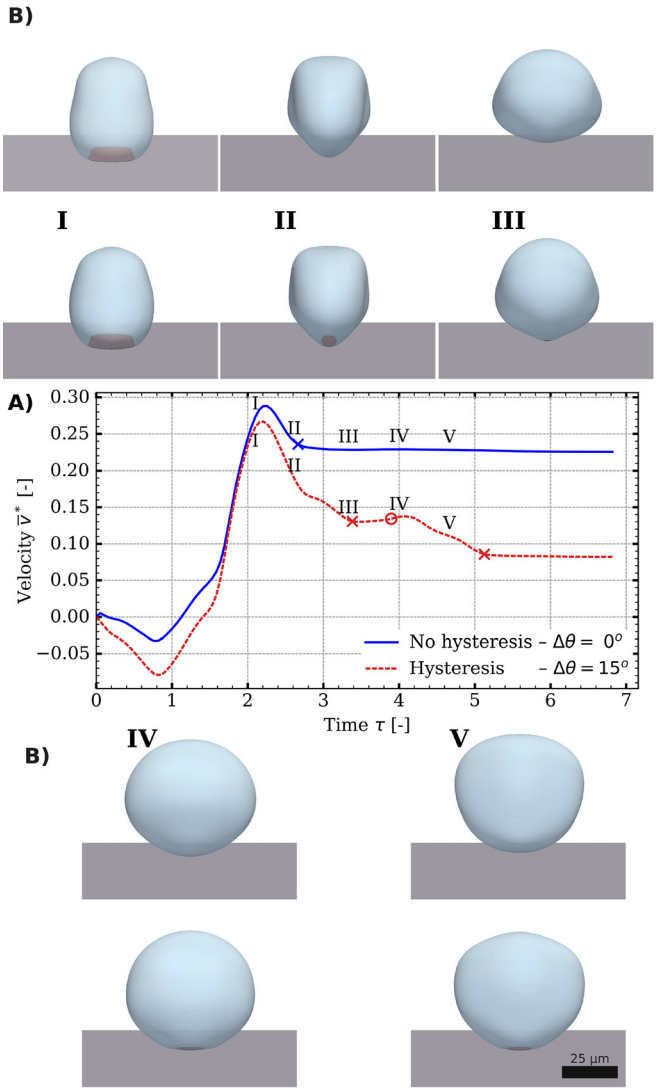

FIG. 7. The influence of hysteresis on fundamental features of droplets jumping from superhydrophobic surfaces. (a) The normalized upward velocities for the hysteresis- and no-hysteresis cases are plotted as a function of non-dimensional time, while the crosses (×) and circles (○) represent the moments where detachment and re-attachment occur correspondingly. (b) Five instants from both simulations are presented. For each pair, the no-hysteresis case is depicted above the corresponding hysteresis one. A significant reduction in the jumping velocity and a temporary re-attachment for the droplets with the hysteresis present is observed. Note the difference in the droplet–surface contact area at instant *II* for the two cases. Droplet sizes are indicated in the bottom of the figure.

The re-attachment is an important finding, contrasting the experience of jumping droplets on no-hysteresis surfaces, where the merged droplet just elevates into the air. At instant *V*, the merged droplet in the hysteresis case has a significantly different shape moment before detaching for the second time. Eventually, the droplet elevates with the reduced upward velocity to that it possessed at the point of the final detachment. The droplet in the no-hysteresis case never experienced re-attachment and kept elevating with a constant velocity, while experiencing damping shape oscillations.

Next, we looked at the sensitivity of the simulations to slight variations of θ_{adv} and θ_{rec}. In addition to our base case, two more cases were tested with (i) a halved hysteresis with $\Delta\theta = 7^\circ$ and (ii) lowering θ_{adv} and θ_{rec} by 4°. In Fig. 8(a), the velocities of these three cases are presented. Figure 8(b) shows the corresponding calculated contact angles imposed in the vicinity of the MCL, averaged for the different cells. The case (i) with a reduced hysteresis showed an increased jumping velocity but the same general behavior of the coming detachment–re-attachment–detachment cycle as the base one. For case (ii) with the reduced contact angles, the merged droplet was unable to jump. The experienced average velocity is below zero, as the droplet finally detaches during a retraction of the MCL caused by the shape oscillation. Since the droplet decelerated during the contact with the surface, it obtained a negative velocity, with the direction being toward the wall. The contact-angle values show that for the base case

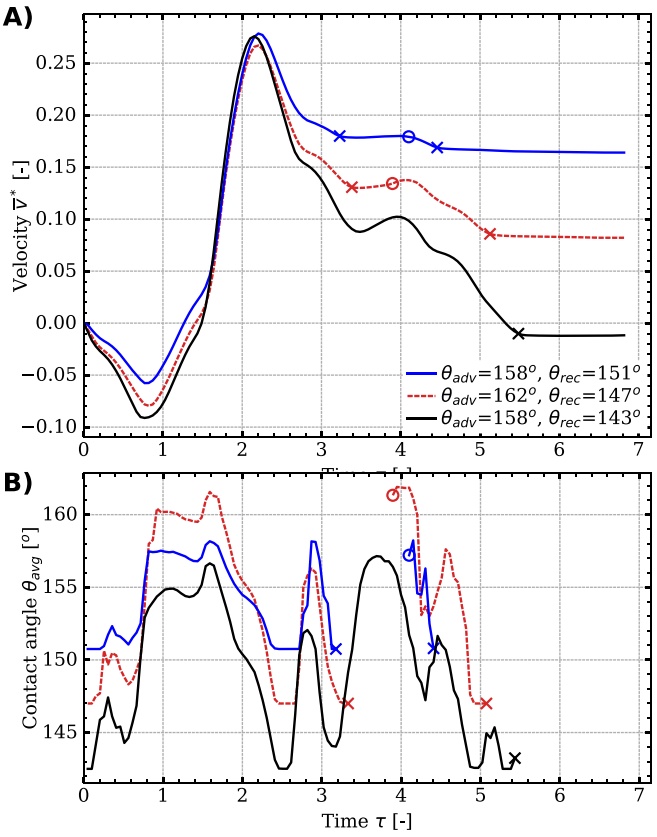

FIG. 8. (a) Velocity evolution of three cases with a substantial hysteresis: the base case (the dashed red line) with $\Delta\theta = 15^\circ$, the test case (i) (the blue line) with a reduced hysteresis ($\Delta\theta = 7^\circ$), and the test case (ii) (the black line) with lower contact angles imposed while preserving $\Delta\theta = 15^\circ$. The initial droplet radius in all the cases is $R_i = 25\,\mu$m. The crosses (×) and circles (○) represent the moments where detachment and re-attachment occur. (b) Variations of the contact angle with time for the three cases, averaged for the length of the contact line. The differences in contacts of the droplets with the superhydrophobic surface are observed, as well as the decrease in the jumping velocity, as the degree of hysteresis increases and/or θ decreases.

the process was initiated with the receding contact angles in most locations of the interface. Following the moment when the liquid bridge hits the surface, the droplet expands on the solid surface and the advancing angles dominate. At that point, high acceleration is observed. Before detachment for the cases with the applied hysteresis, the imposed angles switched twice between the receding and advancing angles. The jumping occurred for the base case and the test case (i). After this, the merged droplet was re-attached with a slight time difference between the two cases, at which point an advancing behavior was observed before ultimately switching to a mostly receding one and finally jumping. The test case (ii) with the lower contact angles showcased similar variations for the contact angle, caused by the shape oscillations of the merged droplet, and eventually, the droplet was detached at a later stage. Additional information is given in Fig. 8(b) on the enhanced attraction of the initial droplets mass toward the solid surface, during the liquid bridge expansion stage. The receding values are dominating the initial stage and the influence in the negative velocity is more prominent for higher hysteresis situations. Moreover, the maximum upward velocity of the merged droplets is roughly the same, which proves that θ_{adv} is a less important factor to the eventual jumping velocity compared to the value for θ_{rec}.

We have seen so far that the presence of hysteresis significantly changes the nature of the jumping process from superhydrophobic surfaces. An interesting question is now the role of the size of initial droplets. In our previous work,[79] it was shown that droplets as small as $R_i = 10\ \mu$m demonstrate the same non-dimensional velocity as do larger droplets, with only gravity becoming a factor of variation in the latter case. Therefore, we have performed a series of simulations with varying droplet radii in which contact angles were given according to the base case ($\Delta\theta = 15^\circ$). Figure 9(a) demonstrates the non-dimensional velocities for $R_i = 12.5$–$200\ \mu$m, which show for all the cases the previously identified re-attachment–detachment phenomenon that follows the initial detachment stage. The jumping velocity decreases for each size reduction. This finding emphasizes that, as the relevance of inertia decreases related to the viscous forces in the system, the droplet will stay attached longer to the surface. Consequently, a longer contact will result in more dissipation of energy due to interaction with the superhydrophobic surface, which in the numerical investigation is partly caused by the viscous stresses at the moving contact line (MCL). To identify the sensitivity of that result to the contact-angle values, the hysteresis was reduced to a half of that of the base case ($\Delta\theta = 7^\circ$, the same as presented in Fig. 8) for all the different sizes and the results are presented in Fig. 9(b). It is noted that for $R_i \geq 100\ \mu$m the droplet is detaching from the surface only once and retains the jumping velocity of the first detachment, in line with the known behavior of cases without hysteresis. For $R_i \leq 50\ \mu$m, the double detachment is observed for both configurations, although a higher jumping velocity is noticed for the cases with a lower degree of hysteresis. The decreased velocity in the cases with higher hysteresis is explained by the greater adhesion force ($F_{pinning}$), as the merged droplet remains longer in contact with the surface.

After having observed the effects of hysteresis when $\Delta\theta$ increases, we looked at the influence of the initial radii (R_i) of the coalescing droplets on the jumping velocity. In detail, we have tested four $\Delta\theta$ (0°, 3°, 7°, and 15°) with five cases of initial droplet radii ($R_i = 12.5$, 25, 50, 100, and 200 μm). The jumping velocities are presented in Fig. 10. We note that the jumping velocities decrease steadily for

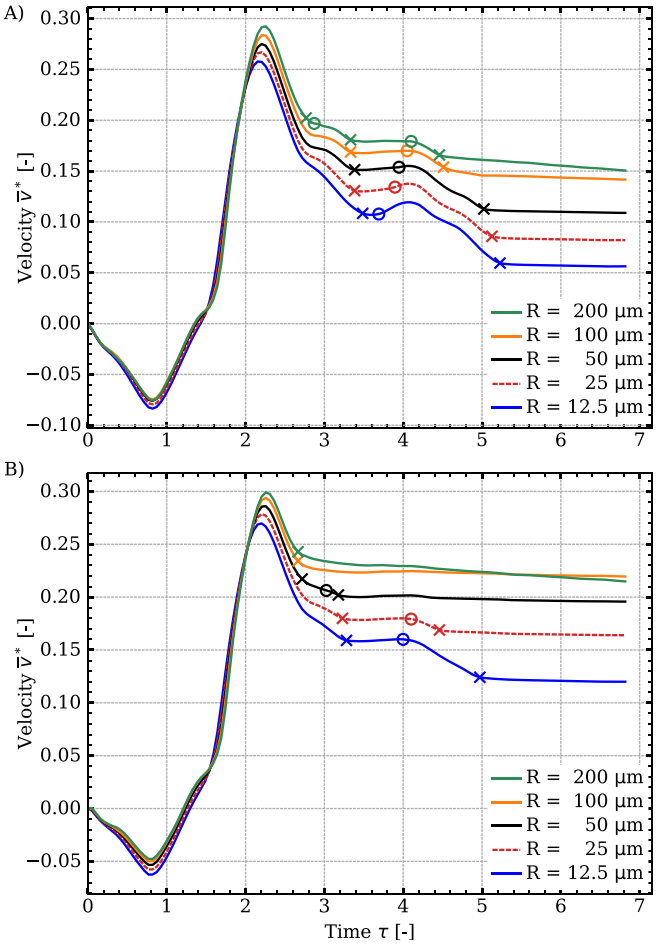

FIG. 9. Effect of radius of the initial droplets on the velocity for cases with different degrees of hysteresis (a) $\Delta\theta = 15^\circ$ with $\theta_{adv} = 162^\circ$ and $\theta_{rec} = 147^\circ$, and (b) $\Delta\theta = 7.5^\circ$ with $\theta_{adv} = 158^\circ$ and $\theta_{rec} = 151^\circ$. The non-dimensional upward velocity of the droplets is compared for five droplet radii. The moments of detachment and re-attachment are pointed with crosses (×) and circles (○), respectively, for each simulation. We notify the trend for the decrease in the jumping velocity as the droplet radius reduces.

droplets smaller than $R_i \leq 50\ \mu$m. Such a trend is particularly visible for the cases with $\Delta\theta = 7^\circ$ and 15°, where the influence of a receding contact angle hinders the self-jumping of droplets of progressively smaller radii. On the other hand, the jumping velocity is much less sensitive to changes in droplet radii for no-hysteresis and small-hysteresis cases (0° and 3°). A slight drop, as observed at $R_i \leq 25\ \mu$m, follows the trends reported in the literature for numerical studies of jumping of microdroplets on superhydrophobic surfaces.[79] There can be two additional conclusions from the same figure. The first one is that the highest degree of hysteresis showed a significant decrease in the jumping velocity for all the radii investigated. Second, there is a significant jump in the decrease in the jumping velocity of the case of $\Delta\theta = 7^\circ$ when R_i lowers from 50 to 12.5 μm. Our understanding is that, considering also the results from Fig. 9, the jumping droplet misses a chance of detaching, while a retraction stage is recorded for

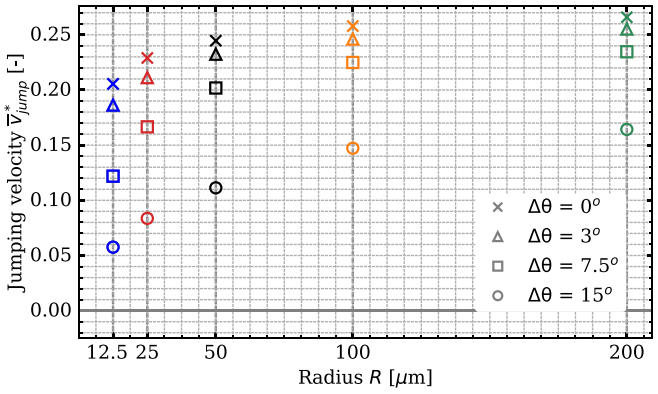

FIG. 10. Collected numerical results for v^*_{jump} over five different initial droplets radii, R_i. The increasing hysteresis leads to a significant reduction in the jumping velocity. This trend is especially pronounced for all the R_i in the highest hysteresis case and for $R_i \leq 50$ μm for the medium hysteresis case (e.g., for $\Delta\theta = 7.5°$).

$R_i \leq 25$ μm, and therefore, it decelerates and has a re-attachment at a later stage, which causes the significant loss of the upward kinetic energy.

As the next step in our study, we looked at the significance of using dynamic contact angles in the simulations. We focused on being able to dynamically adjust the contact angle during its implementation in the cells near the solid surface and in proximity to the contact line location. For this study, θ_{dyn} is dependent on the computed contact line velocity and the model chosen for obtaining θ_{dyn} is the Kistler model,[73] which utilizes the Hoffman correlation function for apparent contact angles in advancing liquids. The same model has also been used when a contact line is receding. A modification of the Hoffman function was implemented following a previous study on both advancing and receding contact angles, which proved that for surfaces with very high contact angles,[75] the Kistler model is still able to capture the behavior of the published experimental data.[74] We remind the reader that when using the Kistler model, the value of the contact angle for a static arrangement is required, which is the same as the quasi-static θ_{adv} and θ_{rec} values for the corresponding contact line movement. In our case, the values of $\theta_{adv} = 162°$ and $\theta_{rec} = 147°$ were used as input when implementing the dynamic contact-angle model. The simulations were performed for two initial droplet radii, $R_i = 25$ μm and $R_i = 200$ μm, and the normalized velocity profiles are shown in Fig. 11. For comparison, we present the results obtained using the quasi-static contact-angle model in the same figure. The velocity decreased for both sizes when using a dynamic model, as the contact period of the merged droplet with the surface lasted longer. For the case of $R_i = 200$ μm with the quasi-static contact-angle model, the merged droplet demonstrated an early detachment–re-attachment sequence, which was not seen in the dynamic contact-angle case, where the merged droplet remained in contact with the solid surface at that point. Afterward, the larger droplet in the dynamic contact-angle model case displayed a delayed final detachment compared to the quasi-static contact-angle one, which resulted in a decrease in the jumping velocity of more than 25%. A similar behavior of a longer contact and the later release was identified for the smaller droplet case, where the use of the dynamic contact-angle model showed a single occurrence of detachment and a highly reduced jumping velocity compared to the

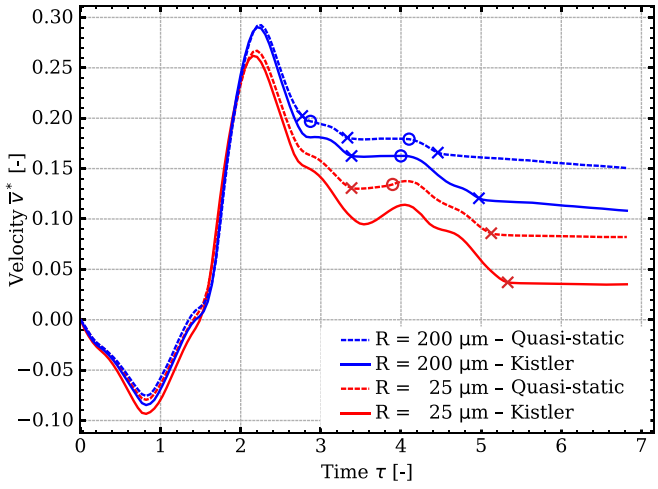

FIG. 11. The normalized velocity using two contact-angle models: the quasi-static model (the dashed lines) and the Kistler dynamic model (the solid lines) for two initial droplet radii R_i. The crosses (×) and circles (○) represent the moments where detachment and re-attachment occur. The normalized velocity plots illustrate how the use of different models affects the upward velocity of the droplets. The use of the Kistler model results in the lower jumping velocity for both R_i.

quasi-static contact-angle case (the difference being more than 40%). We remind the reader here that using the quasi-static contact-angle model already represented a significant step in reducing the jumping efficiency when hysteresis was considered.

Following the results for droplets of $R_i = 25$ μm, in Fig. 12, the averaged contact-angle values along the MCL are given for the two different contact-angle models at each time step. We note how the dynamic contact angle decreases differently in the periods when a more pronounced receding movement of the contact line is observed. The receding contact angle of the dynamic model is lower than the one from the static θ_{rec} during the retraction stages of the merged droplet. This adjustment causes the merged droplet to avoid detachment at

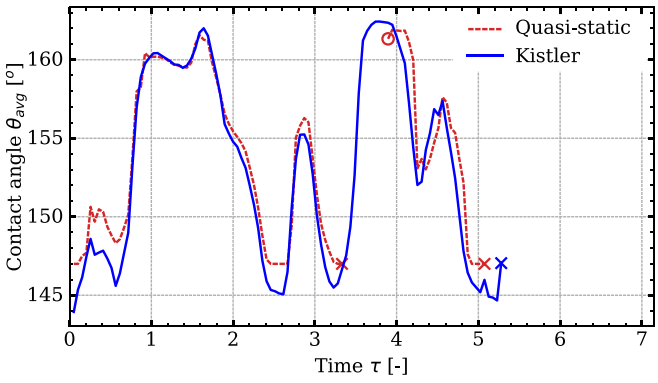

FIG. 12. Comparison of the averaged contact angle implemented along the contact line in the cases of the two contact-angle models for $R_i = 25$ μm. The crosses (×) and circles (○) represent the moments where detachment and re-attachment occur. The use of the Kistler model led to a deviation of the receding contact-angle value that is imposed at the merged droplet. As a result, a longer period of contact to the solid surface was noted.

$\tau \sim 3.4$ in contrast to the quasi-static model case, while it also delays the final detachment of the droplet. This slight variation in the averaged receding contact angle of almost 2°, during the time where the contact line velocity is high, demonstrates variations in possible outcomes of the jumping process and its efficiency. These variations reveal the importance of applying the effective (i.e., truly acting) contact angle and deciding on the choice of parameters that affect the dynamic contact angle, which for our study was the contact line velocity. Note that, in general, there can be other possibilities for such parameters (that were not considered in this study), such as the existence of pillars or partial wetting instabilities (e.g., changes from Wenzel to Cassie–Baxter wetting types).

The choice of a dynamic contact-angle model leads to variations in the velocity evolution and the dependence on the effective receding contact angle in the system. For a more systematic study on how the mentioned phenomena vary for droplets of different sizes, the two contact-angle models were employed in the simulations involving five initial droplet radii ($R_i = 12.5, 25, 50, 100$, and $200\,\mu$m). The results were compared to the equivalent simulations with the static contact angle at $\theta_{st} = 154°$, which is the mean of the θ_{adv} and θ_{rec} for the superhydrophobic surface investigated in this study. The results are presented in Fig. 13. The significant decrease in the jumping velocity, which was already recognized between the cases involving the static and quasi-static contact-angle representations in Fig. 10, was further exaggerated by an extra negative offset, proportional to R_i, when the dynamic contact-angle model was used. More specifically, the jumping velocity obtained by the Kistler model for $R_i \leq 25\,\mu$m droplets is only $10\% - 15\%$ of the jumping velocity for an ideal superhydrophobic surface without hysteresis present. It can be concluded that the presence of a cutoff radius of around $R_i \sim 25\,\mu$m, as recorded by Mulroe *et al.*[31] for the actual surface, is more realistically captured by the simulations with the quasi-static and the Kistler contact-angle model, in contrast to the simulations using the static contact angle. We note here that the Kistler dynamic contact-angle model depends on a relatively limited number of properties, such as the contact line velocity and the liquid properties. Other formulations are always possible; that is, different models can be tested to find correlations that a certain dynamic model can have to a specific superhydrophobic surface.

We have seen that many of the fundamental attributes observed when droplets jump from superhydrophobic surfaces with hysteresis

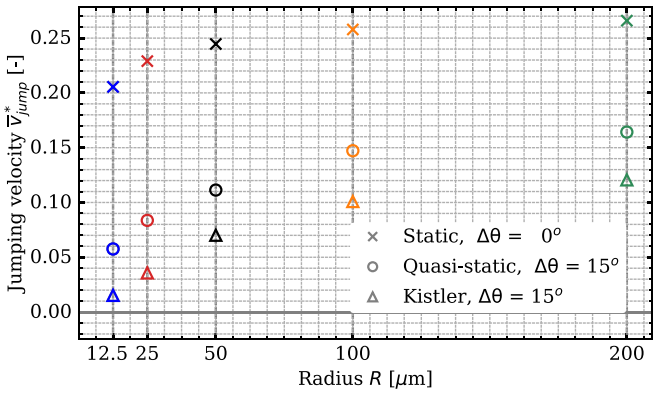

FIG. 13. The jumping velocity as a function of initial droplet radii (R_i) when three contact-angle models were tested. For a surface with a present contact-angle hysteresis, the static contact angle will overpredict the jumping velocity v^*_{jump}.

are directly linked to specific features of the interaction of the merged droplet with a solid surface in such cases. We thus present the contact area evolution A_{cont} obtained by different simulations in Fig. 14(a) to uncover even more subtle effects that are caused by enforcing the contact-angle hysteresis. The variations of contact areas with time are presented in the figure of the cases with a static contact angle, the quasi-static, and the Kistler dynamic contact-angle models. It is shown that, even though the initial evolutions of the contact areas during coalescence are not identical, the liquid bridge impingement and the maximum upward acceleration bear qualitative similarities for the three cases. However, there are subtle differences that explain a different dynamics of the jumping process in the three cases. We see that a minimization of the contact area in the static contact-angle case occurs in a rapid manner, while for the quasi-static and Kistler models, the

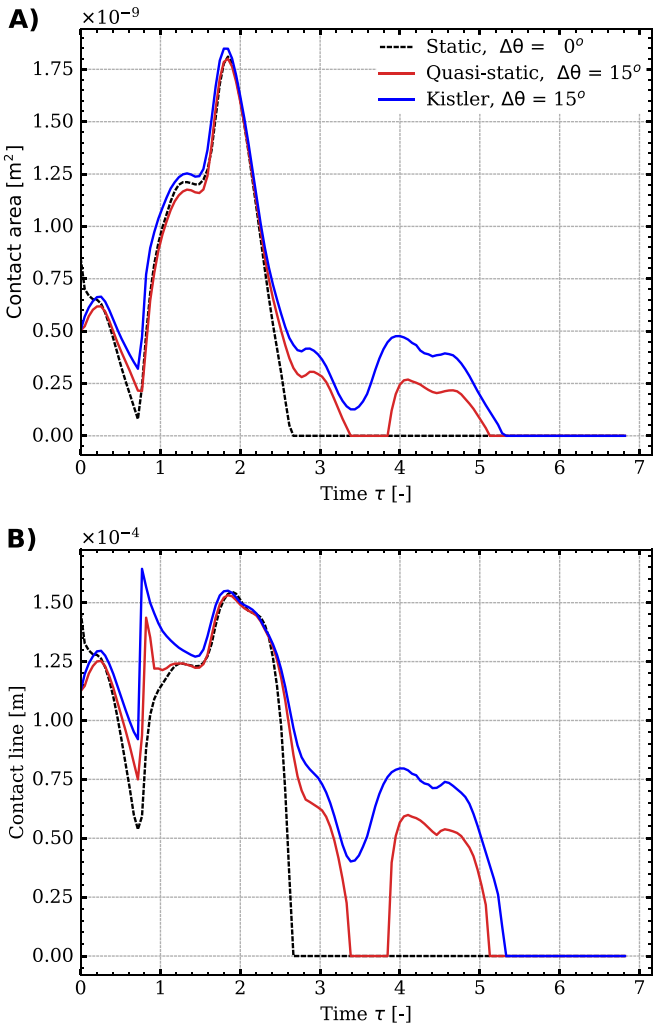

FIG. 14. (a) Contact area evolution and (b) the contact-line length evolution for the merged droplet on the superhydrophobic solid surface. Three different contact-angle implementations with the same equilibrium angle $\theta = 155°$ and the initial droplet radii $R_i = 25\,\mu$m. A higher value of the contact area before the late detachment can be observed when stronger hysteresis is imposed. The contact line follows the same trend, despite a "spike" when the liquid bridge hits the surface.

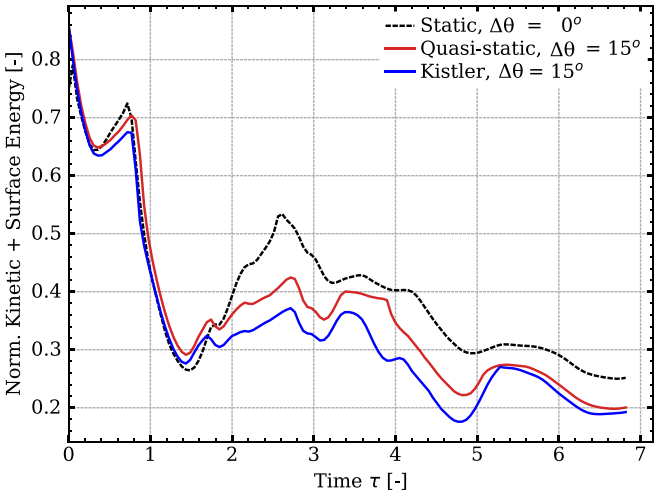

FIG. 15. The sum of the total kinetic energy and the available surface energy from the interface, normalized by the ideal available surface energy (see Sec. IV for more details). Three different cases of contact-angle representations are plotted vs normalized time τ with $R_i = 25\,\mu$m. The difference in the final combined energy between the static contact-angle representation and the quasi-static and Kistler models reveals a higher dissipation for the latter cases.

contact area slows down in reducing and, around the normalized time of $\tau \simeq 3.5$, it starts increasing again. At that moment, the merged droplet starts expanding or re-attaches itself to the surface before a subsequent final retraction and jumping. The length of the contact line, which is given in Fig. 14(b), follows the same trend. A rapid increase at the same instant was observed for the cases that impose hysteresis in the system and is caused by the liquid bridge hitting the surface. The total contact line was already longer in the hysteresis cases when that event occurs something that is attributed to the smaller receding contact angle of the initial spherical droplets when they were in contact with the solid surface.

An increase in the length of the contact line that was previously observed for the case with the dynamic contact-angle model can be directly connected to the presence of higher total stresses in the system. These stresses are exerted from the liquid in the vicinity of the contact line. They cause a higher dissipation of the energy in the system and are attributed to the viscous effect arising from the interaction of the moving interface with the solid surface. To observe the increase in the dissipated energy, we have decided to combine the total kinetic energy K_{tot} and the available surface energy ΔS_{avail}, which is the difference between the instant interface area A_{inter} and the final interface area of the merged droplet A_{end}, multiplied by the gas–liquid surface tension σ [$\Delta S_{avail} = (A_{inter} - A_{end}) \times \sigma$]. We add the two energies and normalize them with the ideal surface energy ΔS_{ideal} of the system, which is the difference between the surface energy of the interface of two initial spherical droplets with R_i (in this case $R_i = 25\,\mu$m) and the resulted merged spherical droplet with a final radius R_{end}. From the equation for the total area of spheres, ΔS_{ideal} is given as $\Delta S_{ideal} = 4\pi(2 \times R_i^2 - R_{end}^2) \times \sigma$. The results from the combined kinetic and interface energy are given in Fig. 15. We understand that the remaining component of the energy budget is completed by the unknown values of the dissipated energy due to viscosity E_{vis} and the surface energy of the contact area between the liquid droplet and the solid surface $S_{cont} = A\,\sigma_{ls}$, for which we know that it will be zero after jumping (σ_{ls} is the surface tension between liquid and the solid surface). The key point in the presented results is given in the final phase of the simulations, where the droplets belonging to all the cases have jumped from the surface. The combined kinetic and surface energy has been more reduced for the cases with hysteresis, with a more prominent reduction for the case with the Kistler model used. Moreover, when we include in the analysis the contact area of Fig. 14(a) for the period that the merged droplet in the hysteresis cases is in contact with the surface, between $\tau \simeq 2.7 - 3.4$ and $\tau \simeq 3.8 - 5.1$, we observe that such cases showcase reduced energy in Fig. 15. A part of this energy is recovered during detachment of the merged droplet, but as the analysis of the final combined energy suggested, the energy is reduced more for the cases with hysteresis.

Finally, we demonstrate different wetting behaviors observed from the quasi-static and the dynamic contact-angle models, following the coalescence of two droplets ($R_i = 25\,\mu$m) at $\tau = 1.58$. In Fig. 16, the contact line is presented in a top view and colored by the local

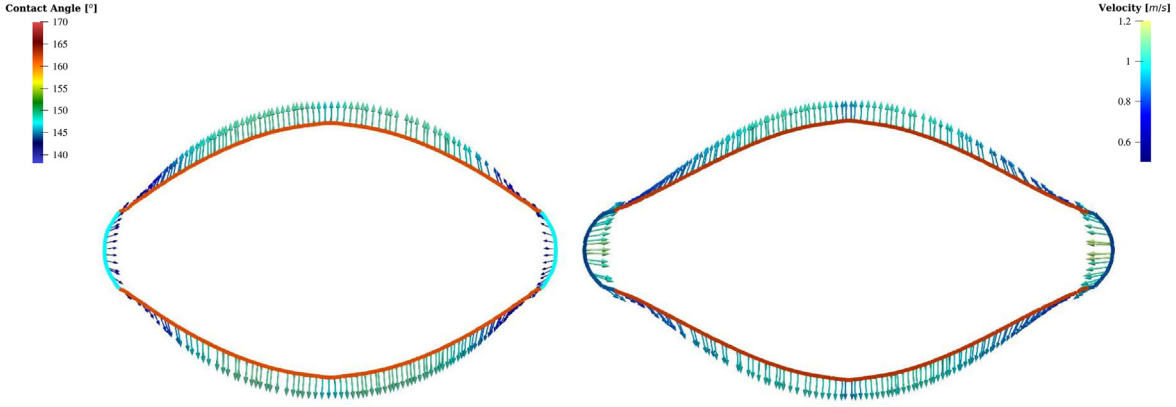

FIG. 16. Outline of the contact area of the merged droplet for the quasi-static contact-angle model (left) and the Kistler dynamic contact-angle model (right), colored by the imposed contact-angle value. We have added vector arrows of the contact line velocity scaled and colored by their magnitude. A significant increase in the contact area is observed, while correlation of the receding movement and the length in the movement's direction is acknowledged.

contact angle imposed along the MCL for each model. The contact line velocity vectors are also depicted. The vector arrows are scaled and colored by their magnitude, and are tangential to the solid surface. At the investigated instant, the contact line of the two simulations shows an advancing movement in the y direction and a receding movement in the x direction. The contact area is significantly increased for the dynamic model (depicted right). However, only the length in the x direction is increased in relation to the one when the quasi-static model is used (left), while the length in the y direction of the contact area is the same. Taking into consideration that the receding angle is some 3° lower for the dynamic model, it permits us to point out the correlation of the lower receding angle to the larger wetting area. In addition, the contact-line velocity in the x direction is higher for the simulation with the dynamic model, which is most likely caused by the higher curvature of the interface near the contact line junction. These outcomes exemplify the highlights of the current study that the jumping process can be highly sensitive to the local contact angle on superhydrophobic surfaces with substantial hysteresis. Therefore, modeling similar cases requires sufficient understanding of the contact-line interaction with the geometrical features of these surfaces.

V. CONCLUSIONS

We primarily focused in this paper on the influence of the contact-angle hysteresis on fundamental features of the jumping process of coalescing droplets on superhydrophobic surfaces, and therefore paid special attention to both representing and numerically implementing effective values of the contact angles acting on such surfaces. A combined VOF–immersed boundary method was used, with an emphasis on the accurate prediction of the moving contact line (MCL) and on the formulation of the corresponding boundary conditions for the contact angles. A series of simulations were performed with static contact angles and dynamic contact-angle models for two equally sized droplets and with several different initial droplet radii. The first outcome of this investigation is that hysteresis causes a delayed merged-droplet release and that it reduces the jumping velocity. Even more importantly, we have identified and explained in detail various forms of events involving droplet detachment and re-attachment to the surface. We have shown that such events depend on the degree of hysteresis for the modeled superhydrophobic surface, with the pinning behavior considerably enhanced when hysteresis was present.

We first demonstrated the temporal and spatial convergence of our numerical framework. The significance was pointed out of carefully selecting an appropriate slip length, as a measure to deal with the contact-line stress singularity. Furthermore, we have tested our framework on the experimentally well-documented case of coalescing and jumping of three unequally sized droplets,[38] and provided great qualitative agreement with experimentally obtained images of all relevant stages of the jumping process. We also showed that we could very well match quantitative results of the jumping velocities over a range of droplet radii. Finally, we have validated our framework with the reported experiments carried out on a superhydrophobic surface with the hysteresis present.[83]

The presence of hysteresis further highlights the differences in the jumping process when different contact-angle representations and models are used. We first compared the case involving a static contact angle and the one with a quasi-static contact-angle model, with the latter using the values of the advancing and receding contact angles. We followed an experimental study,[31] with a reported superhydrophobic surface that predicted the existence of a cutoff radius for the jumping to take place and that is about the size of the simulated droplets. The use of the quasi-static contact-angle model demonstrated a longer period of contact for the merged droplet and the surface, while the jumping velocity was less than a half compared to that when using the static contact-angle. Moreover, the initial detachment of the merged droplet and its subsequent re-attachment to the surface were repeatedly observed, while, eventually, an event of self-ejection occurred.

Two additional investigations with slight variations in the values of the advancing and receding contact angles, together with using a range of different initial droplet radii, portrayed the sensitivity of the simulations to the applied contact angles. Especially after varying the size of the initial droplets, we have observed sequences of detachment and re-attachment, while the final jump took place with a delay in the cases with a higher degree of hysteresis. Similarly, for the smaller droplets, the jumping velocity was observed to decrease, with the moment of jumping being increasingly delayed.

Finally, we used the Kistler dynamic contact-angle model to establish the relevance of using the actual (i.e., effective or truly acting) values of contact angles when studying the jumping process. We compared the obtained results with those when a static contact angle and the quasi-static contact-angle model are used. An investigation of the energy conversion process and the dissipated energy caused by hysteresis was also performed. The analysis supported the conclusion that a dynamic receding contact angle impeded the jumping process, as the jumping velocity became highly reduced or even neutralized for all the tested initial droplet radii. In addition, the duration of the merged droplet–surface contact and the experienced contact area was increased when the dynamic model was used.

ACKNOWLEDGMENTS

The authors would like to thank the Swedish Research Council for the financial support of this project (Vetenskapsrådet, Dnr 2019–04969). In addition, we would like to acknowledge that the handling of data and other computations were enabled by resources provided by the Swedish National Infrastructure for Computing (SNIC), which is partially funded by the Swedish Research Council through Grant Agreement No. 2018–05973.

AUTHOR DECLARATIONS

Conflict of Interest

The authors have no conflicts to disclose.

Author Contributions

Konstantinos Konstantinidis: Conceptualization (equal); Data curation (equal); Formal analysis (equal); Investigation (equal); Methodology (equal); Software (equal); Validation (equal); Visualization (equal); Writing – original draft (equal); Writing – review & editing (equal). **Johan Göhl:** Formal analysis (equal); Methodology (equal); Software (equal); Supervision (equal); Writing – review & editing (equal). **Andreas Mark:** Formal analysis (equal); Methodology (equal); Software (lead); Supervision (equal); Writing – review & editing (equal). **Srdjan Sasic:** Conceptualization (lead); Formal analysis (lead); Funding acquisition (lead); Investigation (lead); Methodology (lead); Project

administration (lead); Resources (lead); Supervision (lead); Validation (lead); Writing – review & editing (lead).

DATA AVAILABILITY

The data that support the findings of this study are available from the corresponding author upon reasonable request.

REFERENCES

[1]D. Quéré, "Non-sticking drops," Rep. Prog. Phys. **68**, 2495–2532 (2005).
[2]N. Miljkovic, R. Enright, and E. N. Wang, "Modeling and optimization of superhydrophobic condensation," J. Heat Transfer **135**, 111004 (2013).
[3]N. Miljkovic, R. Enright, Y. Nam, K. Lopez, N. Dou, J. Sack, and E. N. Wang, "Jumping-droplet-enhanced condensation on scalable superhydrophobic nanostructured surfaces," Nano Lett. **13**, 179–187 (2013).
[4]H. Wang, L. Tang, X. Wu, W. Dai, and Y. Qiu, "Fabrication and anti-frosting performance of super hydrophobic coating based on modified nano-sized calcium carbonate and ordinary polyacrylate," Appl. Surf. Sci. **253**, 8818–8824 (2007).
[5]S. A. Kulinich and M. Farzaneh, "How wetting hysteresis influences ice adhesion strength on superhydrophobic surfaces," Langmuir **25**, 8854–8856 (2009).
[6]S. Farhadi, M. Farzaneh, and S. A. Kulinich, "Anti-icing performance of superhydrophobic surfaces," Appl. Surf. Sci. **257**, 6264–6269 (2011).
[7]L. B. Boinovich and A. M. Emelyanenko, "Anti-icing potential of superhydrophobic coatings," Mendeleev Commun. **23**, 3–10 (2013).
[8]C. Antonini, A. Amirfazli, and M. Marengo, "Drop impact and wettability: From hydrophilic to superhydrophobic surfaces," Phys. Fluids **24**, 102104 (2012).
[9]K. M. Wisdom, J. A. Watson, X. Qu, F. Liu, G. S. Watson, and C.-H. Chen, "Self-cleaning of superhydrophobic surfaces by self-propelled jumping condensate," Proc. Natl. Acad. Sci. **110**, 7992–7997 (2013).
[10]Q. Wang, X. Yao, H. Liu, D. Quéré, and L. Jiang, "Self-removal of condensed water on the legs of water striders," Proc. Natl. Acad. Sci. U.S.A. **112**, 9247–9252 (2015).
[11]D. Maggiolo, M. Seemann, H. Thunman, O. Santos, A. Larsson, S. Sasic, and H. Ström, "Self-cleaning surfaces for heat recovery during industrial hydrocarbon-rich gas cooling: An experimental and numerical study," AIChE J. **65**, 317–325 (2019).
[12]S. P. Dalawai, M. A. Saad Aly, S. S. Latthe, R. Xing, R. S. Sutar, S. Nagappan, C. S. Ha, K. Kumar Sadasivuni, and S. Liu, "Recent advances in durability of superhydrophobic self-cleaning technology: A critical review," Prog. Org. Coat. **138**, 105381 (2020).
[13]C. Yu, S. Sasic, K. Liu, S. Salameh, R. H. Ras, and J. R. van Ommen, "Nature-inspired self-cleaning surfaces: Mechanisms, modelling, and manufacturing," Chem. Eng. Res. Des. **155**, 48–65 (2020).
[14]W. Chen, A. Y. Fadeev, M. C. Hsieh, D. Öner, J. Youngblood, and T. J. McCarthy, "Ultrahydrophobic and ultralyophobic surfaces: Some comments and examples," Langmuir **15**, 3395–3399 (1999).
[15]B. Bhushan and Y. C. Jung, "Wetting, adhesion and friction of superhydrophobic and hydrophilic leaves and fabricated micro/nanopatterned surfaces," J. Phys.: Condens. Matter **20**, 225010 (2008).
[16]D. Öner and T. J. McCarthy, "Ultrahydrophobic surfaces. Effects of topography length scales on wettability," Langmuir **16**, 7777–7782 (2000).
[17]J. Wu, J. Xia, W. Lei, and B. P. Wang, "Advanced understanding of stickiness on superhydrophobic surfaces," Sci. Rep. **3**, 3268 (2013).
[18]Y. Liu and C. H. Choi, "Condensation-induced wetting state and contact angle hysteresis on superhydrophobic lotus leaves," Colloid Polym. Sci. **291**, 437–445 (2013).
[19]D. Quéré, "Wetting and roughness," Annu. Rev. Mater. Res. **38**, 71–99 (2008).
[20]P.-G. de Gennes, F. Brochard-Wyart, and D. Quéré, *Capillarity Wetting Phenomena* (Springer New York, NY, 2004).
[21]J. H. Snoeijer and B. Andreotti, "Moving contact lines: Scales, regimes, and dynamical transitions," Annu. Rev. Fluid Mech. **45**, 269–292 (2013).
[22]R. Weiqing and E. Weinan, "Boundary conditions for the moving contact line problem," Phys. Fluids **19**, 022101 (2007).
[23]J. B. Boreyko and C. H. Chen, "Self-propelled dropwise condensate on superhydrophobic surfaces," Phys. Rev. Lett. **103**, 184501 (2009).
[24]R. Enright, N. Miljkovic, J. L. Alvarado, K. Kim, and J. W. Rose, "Dropwise condensation on micro-and nanostructured surfaces," Nanoscale Microscale Thermophys. Eng. **18**, 223–250 (2014).
[25]N. Miljkovic, R. Enright, and E. N. Wang, "Effect of droplet morphology on growth dynamics and heat transfer during condensation on superhydrophobic nanostructured surfaces," ACS Nano **6**, 1776–1785 (2012).
[26]K. Wang, Q. Liang, R. Jiang, Y. Zheng, Z. Lan, and X. Ma, "Morphology evolution and dynamics of droplet coalescence on superhydrophobic surfaces," AIChE J. **64**, 2913–2921 (2018).
[27]F. Liu, G. Ghigliotti, J. J. Feng, and C.-H. Chen, "Numerical simulations of self-propelled jumping upon drop coalescence on non-wetting surfaces," J. Fluid Mech. **752**, 39–65 (2014).
[28]F. Liu, G. Ghigliotti, J. J. Feng, and C. H. Chen, "Self-propelled jumping upon drop coalescence on Leidenfrost surfaces," J. Fluid Mech. **752**, 22–38 (2014).
[29]K. Yanagisawa, M. Sakai, T. Isobe, S. Matsushita, and A. Nakajima, "Investigation of droplet jumping on superhydrophobic coatings during dew condensation by the observation from two directions," Appl. Surf. Sci. **315**, 212–221 (2014).
[30]C. Lv, P. Hao, X. Zhang, and F. He, "Dewetting transitions of dropwise condensation on nanotexture-enhanced superhydrophobic surfaces," ACS Nano **9**, 12311–12319 (2015).
[31]M. D. Mulroe, B. R. Srijanto, S. F. Ahmadi, C. P. Collier, and J. B. Boreyko, "Tuning superhydrophobic nanostructures to enhance jumping-droplet condensation," ACS Nano **11**, 8499–8510 (2017).
[32]K. Wang, Q. Liang, R. Jiang, Y. Zheng, Z. Lan, and X. Ma, "Self-enhancement of droplet jumping velocity: The interaction of liquid bridge and surface texture," RSC Adv. **6**, 99314–99321 (2016).
[33]H. Vahabi, W. Wang, J. M. Mabry, and A. K. Kota, "Coalescence-induced jumping of droplets on superomniphobic surfaces with macrotexture," Sci. Adv. **4**, eaau3488 (2018).
[34]D. Lu, M. Zhao, H. Zhang, Y. Yang, and Y. Zheng, "Self-enhancement of coalescence-induced droplet jumping on superhydrophobic surfaces with an asymmetric V-groove," Langmuir **36**, 5444–5453 (2020).
[35]Q. Peng, X. Yan, J. Li, L. Li, H. Cha, Y. Ding, C. Dang, L. Jia, and N. Miljkovic, "Breaking droplet jumping energy conversion limits with superhydrophobic microgrooves," Langmuir **36**, 9510–9522 (2020).
[36]M. K. Kim, H. Cha, P. Birbarah, S. Chavan, C. Zhong, Y. Xu, and N. Miljkovic, "Enhanced jumping-droplet departure," Langmuir **31**, 13452–13466 (2015).
[37]Z. Khatir, K. J. Kubiak, P. K. Jimack, and T. G. Mathia, "Dropwise condensation heat transfer process optimisation on superhydrophobic surfaces using a multi-disciplinary approach," Appl. Therm. Eng. **106**, 1337–1344 (2016).
[38]X. Yan, L. Zhang, S. Sett, L. Feng, C. Zhao, Z. Huang, H. Vahabi, A. K. Kota, F. Chen, and N. Miljkovic, "Droplet jumping: Effects of droplet size, surface structure, pinning, and liquid properties," ACS Nano **13**, 1309–1323 (2019).
[39]S. Farokhirad, J. F. Morris, and T. Lee, "Coalescence-induced jumping of droplet: Inertia and viscosity effects," Phys. Fluids **27**, 102102 (2015).
[40]X. Liu and P. Cheng, "3D multiphase lattice Boltzmann simulations for morphological effects on self-propelled jumping of droplets on textured superhydrophobic surfaces," Int. Commun. Heat Mass Transfer **64**, 7–13 (2015).
[41]K. Wang, Q. Liang, R. Jiang, Y. Zheng, Z. Lan, and X. Ma, "Numerical simulation of coalescence-induced jumping of multidroplets on superhydrophobic surfaces: Initial droplet arrangement effect," Langmuir **33**, 6258–6268 (2017).
[42]R. Attarzadeh and A. Dolatabadi, "Coalescence-induced jumping of micro-droplets on heterogeneous superhydrophobic surfaces," Phys. Fluids **29**, 012104 (2017).
[43]J. Wasserfall, P. Figueiredo, R. Kneer, W. Rohlfs, and P. Pischke, "Coalescence-induced droplet jumping on superhydrophobic surfaces: Effects of droplet mismatch," Phys. Rev. Fluids **2**, 123601 (2017).
[44]X. Chen, J. Lu, and G. Tryggvason, "Numerical simulation of self-propelled non-equal sized droplets," Phys. Fluids **31**, 052107 (2019).
[45]S. Li, F. Chu, J. Zhang, D. Brutin, and D. Wen, "Droplet jumping induced by coalescence of a moving droplet and a static one: Effect of initial velocity," Chem. Eng. Sci. **211**, 115252 (2020).

[46]T. Mouterde, T.-V. Nguyen, H. Takahashi, C. Clanet, I. Shimoyama, and D. Quéré, "How merging droplets jump off a superhydrophobic surface: Measurements and model," Phys. Rev. Fluids **2**, 112001 (2017).
[47]F. Chu, Z. Yuan, X. Zhang, and X. Wu, "Energy analysis of droplet jumping induced by multi-droplet coalescence: The influences of droplet number and droplet location," Int. J. Heat Mass Transfer **121**, 315–320 (2018).
[48]Z. Yuan, R. Wu, and X. Wu, "Numerical simulations of multi-hop jumping on superhydrophobic surfaces," Int. J. Heat Mass Transfer **135**, 345–353 (2019).
[49]Y. Wang and P. Ming, "Dynamic and energy analysis of coalescence-induced self-propelled jumping of binary unequal-sized droplets," Phys. Fluids **31**, 122108 (2019).
[50]S. Moghtadernejad, M. Tembely, M. Jadidi, N. Esmail, and A. Dolatabadi, "Shear driven droplet shedding and coalescence on a superhydrophobic surface," Phys. Fluids **27**, 032106 (2015).
[51]H. Hou, Z. Yuan, Z. Hu, S. Gao, and X. Wu, "Effects of the surface tension gradient and viscosity on coalescence-induced droplet jumping on superamphiphobic surfaces," Phys. Fluids **33**, 112101 (2021).
[52]Y. Nam, H. Kim, and S. Shin, "Energy and hydrodynamic analyses of coalescence-induced jumping droplets," Appl. Phys. Lett. **103**, 161601 (2013).
[53]Y. Cheng, J. Xu, and Y. Sui, "Numerical investigation of coalescence-induced droplet jumping on superhydrophobic surfaces for efficient dropwise condensation heat transfer," Int. J. Heat Mass Transfer **95**, 506–516 (2016).
[54]Y. Chen and Y. Lian, "Numerical investigation of coalescence-induced self-propelled behavior of droplets on non-wetting surfaces," Phys. Fluids **30**, 112102 (2018).
[55]Y. Shi, G. H. Tang, and H. H. Xia, "Investigation of coalescence-induced droplet jumping on superhydrophobic surfaces and liquid condensate adhesion on slit and plain fins," Int. J. Heat Mass Transfer **88**, 445–455 (2015).
[56]H. Li, W. Yang, A. Aili, and T. Zhang, "Insights into the impact of surface hydrophobicity on droplet coalescence and jumping dynamics," Langmuir **33**, 8574–8581 (2017).
[57]Z. Liang and P. Keblinski, "Coalescence-induced jumping of nanoscale droplets on super-hydrophobic surfaces," Appl. Phys. Lett. **107**, 143105 (2015).
[58]S. Gao, Q. Liao, W. Liu, and Z. Liu, "Self-removal of multiple and multisize coalescing nanodroplets on nanostructured surfaces," J. Phys. Chem. C **122**, 20521–20526 (2018).
[59]F. F. Xie, G. Lu, X. D. Wang, and D. Q. Wang, "Enhancement of coalescence-induced nanodroplet jumping on superhydrophobic surfaces," Langmuir **34**, 11195–11203 (2018).
[60]Y. Nam, D. Seo, C. Lee, and S. Shin, "Droplet coalescence on water repellant surfaces," Soft Matter **11**, 154–160 (2015).
[61]H. Cha, C. Xu, J. Sotelo, J. M. Chun, Y. Yokoyama, R. Enright, and N. Miljkovic, "Coalescence-induced nanodroplet jumping," Phys. Rev. Fluids **1**, 064102 (2016).
[62]T. Mouterde, G. Lehoucq, S. Xavier, A. Checco, C. T. Black, A. Rahman, T. Midavaine, C. Clanet, and D. Quéré, "Antifogging abilities of model nanotextures," Nat. Mater. **16**, 658–663 (2017).
[63]E. B. Dussan, "On the spreading of liquids on solid surfaces: Static and dynamic contact lines," Annu. Rev. Fluid Mech. **11**, 371–400 (1979).
[64]P. G. De Gennes, "Wetting: Statics and dynamics," Rev. Mod. Phys. **57**, 827–863 (1985).
[65]D. Legendre and M. Maglio, "Comparison between numerical models for the simulation of moving contact lines," Comput. Fluids **113**, 2–13 (2015).
[66]J. Eggers and H. A. Stone, "Characteristic lengths at moving contact lines for a perfectly wetting fluid: The influence of speed on the dynamic contact angle," J. Fluid Mech. **505**, 309–321 (2004).
[67]S. Afkhami, J. Buongiorno, A. Guion, S. Popinet, Y. Saade, R. Scardovelli, and S. Zaleski, "Transition in a numerical model of contact line dynamics and forced dewetting," J. Comput. Phys. **374**, 1061–1093 (2018).
[68]J. Göhl, A. Mark, S. Sasic, and F. Edelvik, "An immersed boundary based dynamic contact angle framework for handling complex surfaces of mixed wettabilities," Int. J. Multiphase Flow **109**, 164–177 (2018).
[69]A. Mark, R. Rundqvist, and F. Edelvik, "Comparison between different immersed boundary conditions for simulation of complex fluid flows," Fluid Dyn. Mater. Process. **7**, 241–258 (2011).
[70]J. P. Van Doormaal and G. D. Raithby, "Enhancements of the simple method for predicting incompressible fluid flows," Numer. Heat Transfer **7**, 147–163 (1984).
[71]O. Ubbink and R. I. Issa, "A method for capturing sharp fluid interfaces on arbitrary meshes," J. Comput. Phys. **153**, 26–50 (1999).
[72]J. U. Brackbill, D. B. Kothe, and C. Zemach, "A continuum method for modeling surface tension," J. Comput. Phys. **100**, 335–354 (1992).
[73]S. Kistler, "Hydrodynamics of wetting," *Wettability* (CRC Press, 1993), pp. 310–430.
[74]R. L. Hoffman, "A study of the advancing interface. II. Theoretical prediction of the dynamic contact angle in liquid-gas systems," J. Colloid Interface Sci. **94**, 470–486 (1983).
[75]M. Jiang and B. Zhou, "Improvement and further investigation on Hoffman-function-based dynamic contact angle model," Int. J. Hydrogen Energy **44**, 16898–16908 (2019).
[76]M. M. Francois, S. J. Cummins, E. D. Dendy, D. B. Kothe, J. M. Sicilian, and M. W. Williams, "A balanced-force algorithm for continuous and sharp interfacial surface tension models within a volume tracking framework," J. Comput. Phys. **213**, 141–173 (2006).
[77]P. Bartholomew, F. Denner, M. H. Abdol-Azis, A. Marquis, and B. G. van Wachem, "Unified formulation of the momentum-weighted interpolation for collocated variable arrangements," J. Comput. Phys. **375**, 177–208 (2018).
[78]A. Mark and B. G. van Wachem, "Derivation and validation of a novel implicit second-order accurate immersed boundary method," J. Comput. Phys. **227**, 6660–6680 (2008).
[79]K. Konstantinidis, J. Göhl, A. Mark, and S. Sasic, "Coalescence-induced jumping of microdroplets on superhydrophobic surfaces—A numerical study," Can. J. Chem. Eng. (published online 2022).
[80]F. Denner and B. G. van Wachem, "Numerical time-step restrictions as a result of capillary waves," J. Comput. Phys. **285**, 24–40 (2015).
[81]M. Renardy, Y. Renardy, and J. Li, "Numerical simulation of moving contact line problems using a volume-of-fluid method," J. Comput. Phys. **171**, 243–263 (2001).
[82]S. Afkhami, S. Zaleski, and M. Bussmann, "A mesh-dependent model for applying dynamic contact angles to VOF simulations," J. Comput. Phys. **228**, 5370–5389 (2009).
[83]X. Yan, Z. Huang, S. Sett, J. Oh, H. Cha, L. Li, L. Feng, Y. Wu, C. Zhao, D. Orejon, F. Chen, and N. Miljkovic, "Atmosphere-mediated superhydrophobicity of rationally designed micro/nanostructured surfaces," ACS Nano **13**, 4160–4173 (2019).